Nonisothermal drop impact and evaporation on polymer nanofiber mats

Christina M. Weickgenannt,[1,2] Yiyun Zhang,[3] Andreas N. Lembach,[1,2] Ilia V. Roisman,[1,2] Tatiana Gambaryan-Roisman,[2,4] Alexander L. Yarin,[2,3,*] and Cameron Tropea[1,2,†]

[1]*Institute of Fluid Mechanics and Aerodynamics, Technische Universität Darmstadt, D-64287 Darmstadt, Germany*

[2]*Center of Smart Interfaces, Technische Universität Darmstadt, D-64287 Darmstadt, Germany*

[3]*Department of Mechanical and Industrial Engineering, University of Illinois at Chicago, MC 251, Chicago, Illinois 60607-7022, USA*

[4]*Institute for Technical Thermodynamics, Technische Universität Darmstadt, D-64287 Darmstadt, Germany*

(Received 20 September 2010; revised manuscript received 5 December 2010; published 11 March 2011)

The work describes the experimental and theoretical investigation of water drop impact onto electrospun polymer nanofiber mats deposited on heated stainless-steel foils. The measurements encompass water spreading over and inside the mat, as well as the corresponding thermal field. The results show that the presence of polymer nanofiber mats prevents receding motion of drops after their complete spreading and promotes the moisture spreading inside the mat over a large area of the heater, which facilitates a tenfold enhancement of heat removal as the latent heat of drop evaporation.

DOI: 10.1103/PhysRevE.83.036305 PACS number(s): 47.55.dr, 44.35.+c, 47.56.+r

I. INTRODUCTION

The continuously rising demand for faster central processing units, the miniaturization and breakthrough developments in the field of semiconductors, optical and radiological components, and the emergence of unmanned aerial and ground vehicles (UAVs and UGVs) result in a growing need for more powerful cooling technologies. These must be capable of removing heat fluxes of up to 1 kW/cm^2. Among the different approaches to cooling, which include, for example, natural and forced convection, heat pipes, or microchannel heat sinks, spray cooling is presently one of the most promising methods [1–7]. The tremendous cooling potential of spray cooling is associated with liquid evaporation at the hot surface. Thereby the efficiency is strongly affected by the hydrodynamics and heat transfer associated with drop impact onto hot surfaces. However, the typical receding motion of the spread-out liquid lamellae on hot metal surfaces leads to complete drop bouncing and interruption of cooling in many cases. Moreover, owing to the insulating vapor layer established between the drop and the surface, the heat flux reduces significantly in the Leidenfrost regime at higher temperatures.

A novel approach in drop and spray cooling of microelectronic devices employs coating of hot surfaces with electrospun nonwoven polymer nanofiber mats [8,9]. Electrospun nanofiber mats are nanotextured permeable materials comprising individual polymer nanofibers (with diameter of approximately several hundred nanometers) that are randomly orientated in the mat plane. The size of the interfiber pores is of the order of several micrometers, and mat thickness can be several hundred micrometers. The electrospun nanofiber mats are usually produced from polymers that are either partially wettable or nonwettable [10,11].

The benefits of using nanofiber mats in drop and spray cooling applications are mainly based on their influence on the hydrodynamic behavior of the impacting drops, as well as an increased heat transfer area. Previous observations showed essentially two significant features of drop impact on nanofiber mats [9]. First of all, receding, splashing, and bouncing during the impact on polymer nanofiber mats seem to be practically eliminated. Drop spreading after impact is similar to that on an impermeable surface, but the drop contact line is pinned as the maximum spread diameter is reached. Second, drop spreading is accompanied by a filling of the pores, which are almost instantaneously impregnated underneath the area encircled by the pinned contact line. Pores continue to be filled after the contact line has been arrested, and liquid spreads inside the nanofiber mat over an area significantly larger than the one encircled by the pinned contact line. Both features lead to an enhancement of heat transfer owing to the enlargement of the contact area between water and the underlying hot surface. Moreover, nanofiber mats possess a tremendously large surface area of $\sim 10^5$ cm^2/g, which also facilitates heat removal.

The present work aims at a detailed elucidation of the drop spreading behavior above and inside nanofiber mats. The evolution of the wetted spot (the water spreading area inside nanofiber mats after drop impact), the corresponding temperature distribution at the heated foil, as well as the evaporation time have been measured for different thicknesses of the mats, different initial temperatures of the hot surface, and different drop impact velocities. A physical interpretation of the results and physical insights into the governing mechanisms are also provided.

II. EXPERIMENTAL METHOD AND DATA PROCESSING

A. Experimental setup

Nanofiber mats used in the present experiments were electrospun from PAN [poly(acrylonitrile)], a partially wettable polymer with a water contact angle on a cast sample of $\sim$30–40 °C and from PAN containing carbon black nanoparticles (CB), which tends to increase the roughness of individual nanofibers [12]. Square samples of nanofiber mats with a side length of $\sim$4 cm, thickness of the order of several hundred micrometers, and porosity of the order of 90%–95% were produced. Nanofiber mats were electrospun on stainless-steel

*ayarin@uic.edu

†ctropea@sla.tu-darmstadt.de

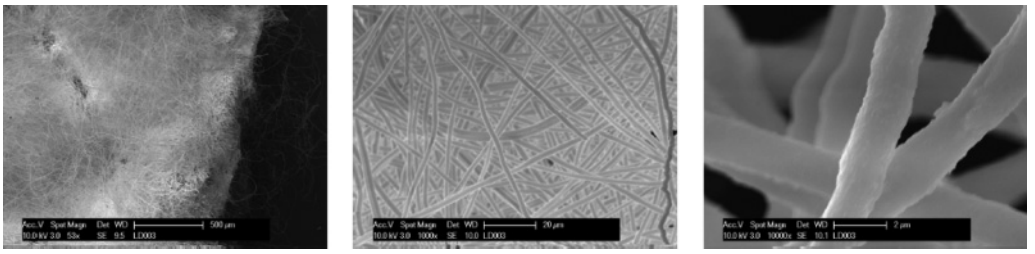

FIG. 1. Scanning electron microscope images of PAN nanofibers at various magnifications. Scale bars are 500 μm, 20 μm and 2 μm, respectively from left to right.

foils attached to a grounded electrode. The thickness of the foils was 50 μm. The electrospinning process is described elsewhere [10,11,13]. Typical scanning electron microscope images of the nanofibers used in the experiments are shown in Figs. 1 and 2.

A schematic diagram of the experimental setup for drop impact is shown in Fig. 3. It consists of the following main elements: drop generation system, impingement surface (stainless-steel foil covered by a nanofiber mat), heating system, high-speed imaging and illumination system, and an infrared (IR) imaging system. For drop generation a medical syringe with a stainless-steel needle was used. The needle was flat tipped. The syringe was manually operated in such a way that a drop could form at the needle tip, detach under its own weight, and be accelerated by gravity. The initial drop diameter was $d_0 = 2 \pm 0.3$ mm. The syringe was fixed at a vertical adjusting spindle, which allowed varying the height of the needle tip over the target surface. The varied impact heights were $H = 5$, 15, and 50 cm, which correspond to the following impact velocities, respectively: $V_0 \approx 1$, 1.7, and 3 m/s.

The stainless-steel foils covered by nanofiber mats were heated electrically. The lower surfaces of the foils have been coated with black graphitic spray. Such coating improves the temperature measurement of the foil using the IR technique. A special mounting device provided continuous stretching of the foil, necessary for compensation of the effects related to the foil thermal expansion at elevated temperatures. The mounting device also incorporated an integrated electric heating system. To ensure small contact resistance, copper plates pressed on the foil from below were used as connections.

A high-speed CCD camera (Photron's Fastcam 1024 PCI) with a frame rate of 1000 fps recording at 1024×1024 image resolution was used to observe the shape of the spreading drop above the hot surface and to measure the initial drop diameter and impact velocity. The camera was aligned at an angle of 40° with respect to the horizontal. The observability of the subsequent drop spreading inside the nanofiber mats depends on several conditions. In general, the refractive indices of the polymer nanofibers and water are such that if a certain level of moisture concentration is reached in the nanofiber mat, it becomes transparent and the underlying darker steel surface becomes visible through the nanofiber mat. Then, water spreading inside the nanofiber mat can be observed as a growing dark area. However, this method is only successful for relatively thin mats and fails in the case of thicker mats [9].

For this reason a second observation technique was used in these experiments. An IR camera (Thermosensorik's CMT 256 M HS) with a refresh rate of 885 Hz in full-frame mode and thermal resolution of <10 mK was positioned underneath the targets and recorded the temperature distribution at the reverse side of the steel foils. The moisture contained inside the mat evaporates, leading to the foil cooling. Because the foils are very thin (50 μm), the moisture-containing area of the mats coincided with the cooled area of the steel foil at any time instant of the water spreading (see Sec. II C). In this way the liquid spreading could be identified for various mat thicknesses. The two cameras, CCD and IR, were synchronized to achieve simultaneous drop imaging and thermal measurements.

The data from the images were analyzed by using an image processing code programmed in Matlab. For this purpose the raw data of the IR camera were converted into temperature levels using calibration curves for each foil used. The image intensity was assumed to be related to the radiation heat flux

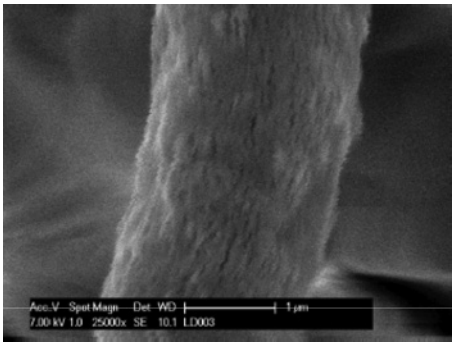

FIG. 2. Scanning electron microscope image of a PAN fiber containing carbon black nanoparticles. Scale bar is 1 μm.

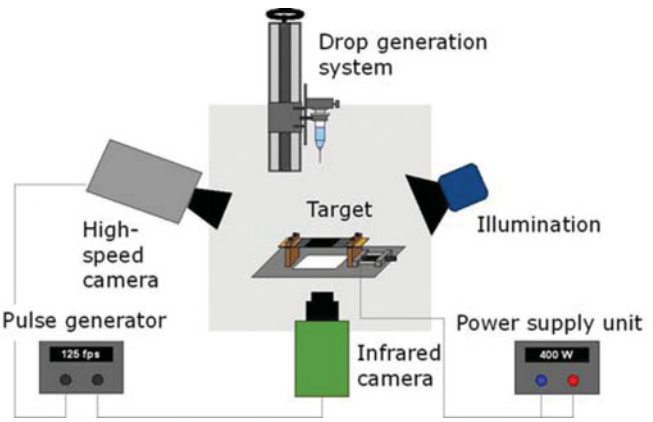

FIG. 3. (Color online) Experimental setup for drop impact onto nanofiber mats.

when using the raw data and temperature curve. According to the Stefan-Boltzmann law, the heat flux transferred from a hot body to a cold body is proportional to the difference of the fourth powers of the surface temperatures. The 1/4 power law was thus chosen to fit the calibration data.

A series of experiments were performed using the setup described at initial foil temperatures ranging from 60 to 120 °C with an increment of 20 °C. Each drop impact experiment started after the foil (heated by the electric current) reached a steady temperature. For the measurement of the initial foil temperature, an external, calibrated thermocouple, which was pressed manually onto the foil, was used. For each foil and at each temperature a reference sequence was first recorded, which was needed for the computation of the calibration curves to convert the raw intensity data of the IR camera into temperature values. After that, a single drop impacted onto the nanofiber mat and the entire spreading and evaporation process was recorded at a low frequency of 125 Hz, simultaneously by both camera systems (CCD and the IR camera). Additionally, the drop impact sequence was recorded only by the CCD camera with a frequency of 30 000 Hz.

The thermal resolution of the IR camera was limited by a temperature of 120 °C. At higher foil temperatures (up to 300 °C) a single thermocouple of type *K* with a diameter of 0.5 mm was used for temperature measurements. It was positioned directly underneath the impact point of the drop and fixed mechanically, which resulted in a measuring error of ∼4 ° C. The experimental procedure was the same as described before.

B. Typical phenomena of drop impact, spreading, and evaporation

Figure 4 shows typical CCD images of drop impact on a bare steel foil as well as on a steel foil coated with a PAN nanofiber mat of thickness $h = 1.05$ mm. In both cases (bare steel and steel coated with nanofibers) the initial foil temperature was ∼60 °C and the drop impact height was $H = 15$ cm. The drop impact onto a smooth bare steel substrate is followed by spreading and receding of liquid over the surface as expected [14] (see Fig. 4, top). After the receding stage the liquid drop reaches a quasi-steady state. The observed behavior during the first few milliseconds after drop impact onto a nanofiber mat is very similar to that in the case of a bare steel foil (see Fig. 4, bottom). The drop first spreads on the polymer mat as on a dry and impermeable smooth rigid surface. However, at the end of the spreading stage the contact line of the drop appears to be pinned in the spread-out configuration and does not recede [9].

Figure 5 demonstrates the differences between drop evaporation on a bare steel foil and on a steel foil coated with a nanofiber mat. Five typical CCD frames and the corresponding IR images from below are shown. Owing to the low recording frequency of 125 Hz, the initial stage of drop impact could not be observed in full detail. The nanofiber mat, the initial foil temperature, as well as the impact height were the same as in the example shown in Fig. 4. In the case of a bare steel foil, the drop reached a quasi-steady state after the initial liquid motion came to rest, as is seen in Fig. 5(a.1). In the following process, the drop contact line remains practically pinned over a significant fraction of the drop lifetime. In contrast to that, the drop height and the contact angle both continually decrease, because of the mass loss owing to evaporation. Only near the end of the evaporation process does the contact line show an appreciable shrinkage. The temperature of the cooled area underneath the drop stays nearly constant as long as the evaporation lasts, as it can be seen in Figs. 5(a.3)–(a.5).

Figure 5(b.1) shows the end of the spreading stage after drop impact on the nanofiber mat, when the contact line of the drop is pinned in the spread-out configuration. The corresponding image of the temperature field demonstrates that, at this early stage after drop impact, an evenly cooled area underneath the drop has not developed yet. Water penetration through the nanofiber mat thickness is not complete.

The entire process can be subdivided into three phases, which were observed for all polymer nanofiber mats used in these experiments. The first phase corresponds to the growth of the cooled area. After the spreading stage is over, the temperature of the back side of the foil is significantly reduced.

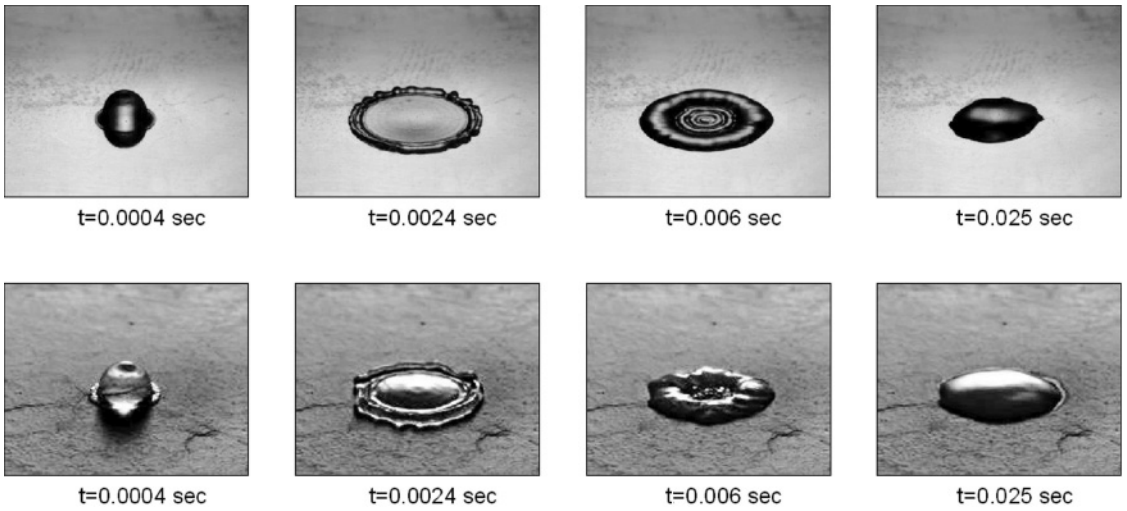

FIG. 4. Drop impact on a bare steel foil and on a nanofiber mat at a foil temperature of 60 °C. Top: bare steel; bottom: steel foil covered with a PAN nanofiber mat (mat thickness $h = 1.05$ mm).

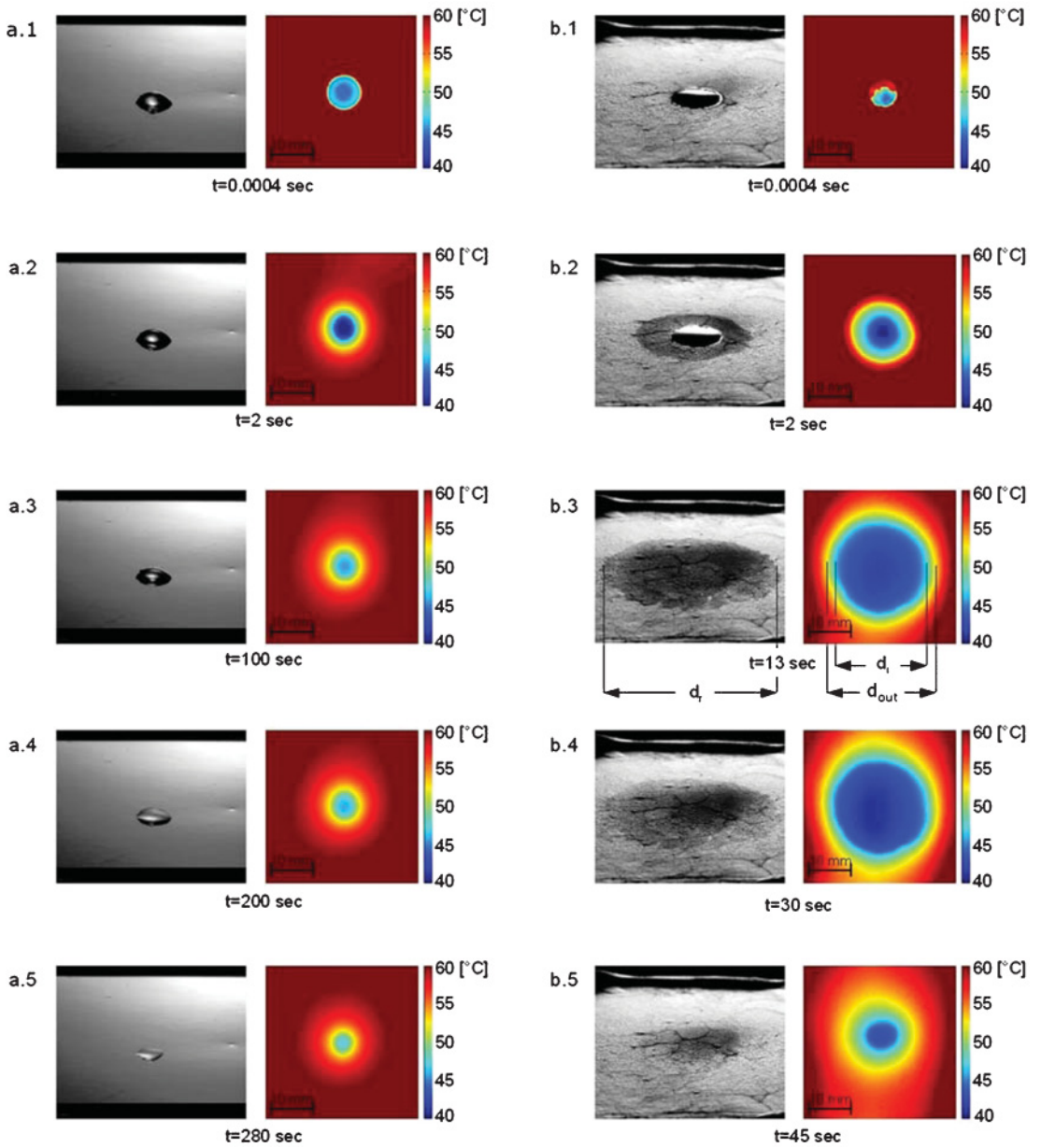

FIG. 5. (Color) Drop evaporation on a steel foil and on a nanofiber mat: (a.1)–(a.5) bare steel; (b.1)–(b.5) steel covered with a PAN nanofiber mat (mat thickness $h = 1.05$ mm). Scale bar is 10 mm.

However, the liquid does not remain at rest after the drop contact line had been pinned but rather starts to spread in the nanofiber mat outside the area encircled by the contact line, as can be seen in Fig. 5(b.2). Water spreading inside the mats occurs in an almost axisymmetric manner. The maximum diameter of the cooled area in the case shown in Fig. 5 is ∼12 times larger than the preimpact diameter of the drop and takes a value of ∼24 mm. During this process, the temperature of the foil underneath the wetted area of the nanofiber mat continues to change. Namely, the growth of the wetted area inside the nanofiber mats leads to a continuous reduction of temperature of the cooled area. When a maximum size of the wetted spot has been achieved, the temperature attains a constant low value that is nearly uniform over the entire cooled area [see the image in Fig. 5(b.3)].

In the following second stage, the evaporation process is comparable to that taking place on an uncoated foil. For the case shown in Fig. 5, the maximal size of the wetted spot does not change during ∼20 s and the temperature of the cooled area does not change significantly either. During this time the intensity of the dark-colored area visible in the high-speed images in Figs. 5(b.3) and 5(b.4) is reduced, which indicates that an additional evaporation cooling occurs over the entire wetted area.

The shrinkage of the cooled area, which corresponds to the shrinkage of the wetted spot, signifies the third and last phase of drop evaporation on a nanofiber mat. After reaching a low threshold of moisture content, the wetted area begins to shrink while the temperature of the cooled area still does not change. The observations at this stage would not have been possible

without using an IR camera. Because the darker coloring of the wetted area in the CCD images fades with increasing time, the complete evaporation process cannot be observed using this as an indicator. The IR images allow one to observe that the shrinkage process occurs continuously, as documented by a monotonous reduction of the diameter of the cooled area. The shrinkage was practically axisymmetric, which corresponds to the most intensive evaporation over the wetted spot perimeter.

If one compares the evaporation process on a bare steel foil and the foil coated with nanofibers, three differences can be observed. First, the cooled area is approximately four times larger with the nanofiber mat than on the uncoated foil. Second, the minimum temperature at which the evaporation occurs is $\sim 7\,^{\circ}$C lower for the nanofiber mat than for the bare steel foil Third, the evaporation time is approximately six times shorter on the nanofiber mat for the same drop size.

C. Definition of the characteristic spreading diameter

The drop spreading inside nanofiber mats was determined on the basis of the IR images. Owing to the thermal conduction in the foil, the decrease of the foil temperature occurs not only underneath the locally wetted area where evaporation takes place but also in the surrounding area. Therefore, a comparison of the visible wetted area in the CCD images and the temperature field images was necessary in order to identify the correct borders of the cooled area corresponding to the wetted spot.

In Fig. 6 three different diameters selected for the comparison are shown; d_r is the diameter of the visible wetted area in the CCD images, and d_i and d_{out} are the diameters of the two most significant temperature differences in the IR images. They were measured manually for ten frames and plotted against time. This procedure was repeated for three measurements on different foils to verify the results. Figure 6 demonstrates that the diameter of the optically visible wetted area recorded by the CCD camera (d_r) corresponds in the IR images to the inner diameter d_i of the intense dark area, i.e., of the area that is cooled down to an almost uniform low temperature. It can be assumed that the evaporation is taking place in this area and that the further temperature reduction in the surrounding area (d_{out}) is caused by thermal conduction in the foil.

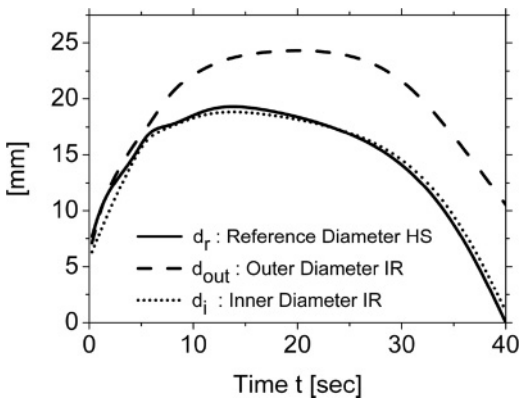

FIG. 6. Comparison of diameters of the wetted area evaluated using the high-speed (HS) and infrared (IR) images. The diameters d_r, d_{out}, and d_i are defined in Fig. 5(b.3).

A fixed threshold was chosen to convert the images from the IR camera to determine a typical diameter of the wetted spot. It is emphasized that this procedure was not used during the initial phase when the water from the drop was still filling the pores directly at the impact location. The duration of that phase was in the range of 0.02–0.3 s after drop impact for different mat thicknesses. For this time span, the diameter was set to zero, which explained the steep increase of d_i at the early stage after drop impact in Fig. 6.

III. EXPERIMENTAL RESULTS AND DISCUSSIONS

A. Water spreading inside nanofiber mats

The hydrodynamics of drop impact on nanofiber mats is essentially characterized by two features: the pinning of the contact line in the spread-out configuration and the further drop imbibition of pores outside the area encircled by the contact line. To elucidate peculiarities of the latter in more detail, the mat thickness, the initial foil temperature, and the drop impact velocity were varied in the experiments. In the following, the diameter of the wetted area is scaled by the initial drop diameter d_0, $d_n = d/d_0$, whereas time t is measured from the drop impact moment. The experiments were performed with nanofiber mats of thicknesses in the range from $h = 0.25$ to 1.05 mm for the PAN samples, and from $h = 0.15$ to 1.75 mm for the PAN + CB samples.

The phenomenon of water imbibition in the nanofiber mats has been observed for all samples used. In all cases water spread almost axisymmetrically, with the maximum spreading diameters in the range $d_{n,\max} = 9$–15. The imbibition kinetics was different for various mats. That manifested itself in different time intervals required to reach $d_{n,\max}$, different values of the full spread-out diameter $d_{\max}$, as well as in different overall time spans for complete evaporation. To demonstrate this, four examples have been chosen. The nanofiber mats are, correspondingly, PAN samples of the thicknesses $h = 0.25$, 1.05, and 1.5 mm, as well as a very thin PAN + CB sample of the thickness of $h = 0.15$ mm.

In Fig. 7 the curves $d^2(t)$ and $d[d^2(t)]/dt$ illustrate the evolution of the cooled area (divided by $\pi/4$) at an initial foil temperature of 60 °C. It is seen that the spreading scenarios are similar for the different mat thicknesses. The spreading inside the mats begins with a high velocity, which then continuously decreases until the spreading diameter reaches its maximum. In the following, the spreading diameter stays at a plateau, whereas the spreading velocity is almost zero. The shrinkage of the cooled area begins then with a low velocity magnitude, which increases with decreasing of the area.

The shortest process was observed for the thinnest mat produced from PAN + CB with a thickness of $h = 0.15$ mm. In that case the entire evaporation process took $\sim$48 s, while it takes nearly 300 s on a bare steel foil under the same experimental conditions. The maximum spread-out diameter of the cooled area in the case of $h = 0.15$ mm was $\sim$15 times larger than the preimpact drop diameter, which corresponds to $d_{\max} = 30$ mm. The time span corresponding to the plateau in $d^2(t)$ was $\sim$20 s. A similar result was obtained for the PAN nanofiber mat with a thickness of $h = 1.05$ mm. In the latter case, the maximum spreading diameter $d_{\max}$ was

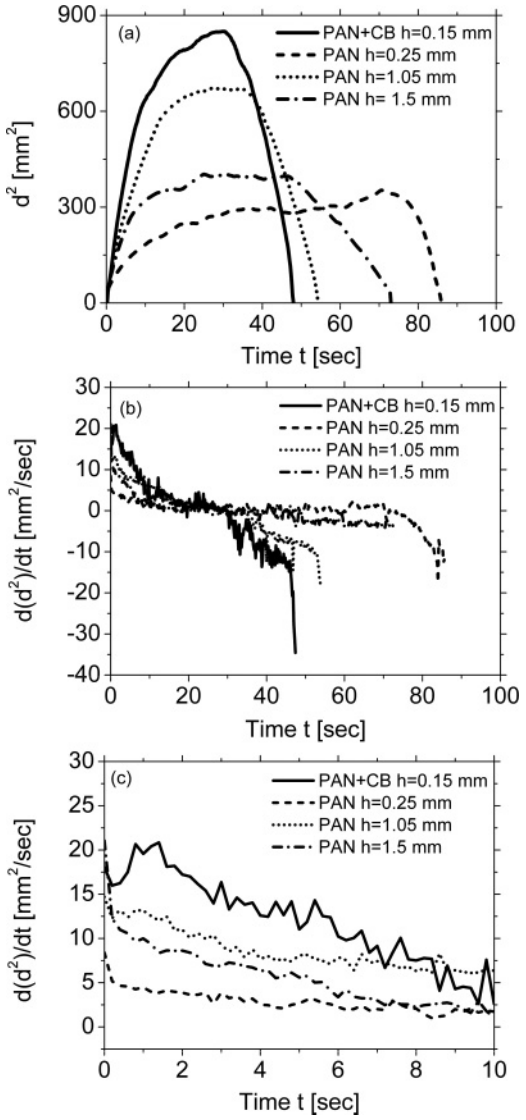

FIG. 7. Evolution of the cooled area (divided by $\pi/4$) in time at an initial foil temperature of 60 °C. (a) d^2 vs time. (b) The derivative $d(d^2)/dt$ vs time. (c) The initial interval of $d(d^2)/dt$ zoomed in.

~12 times larger than the initial drop diameter d_0, the time span corresponding to the plateau in $d^2(t)$ was ~30 s, and the entire evaporation time was ~55 s. In the case of the thickest PAN mat with $h = 1.5$ mm the maximum diameter of the wetted spot was ~9 times larger than the preimpact drop diameter d_0, the time span corresponding to the plateau was ~40 s, and the entire evaporation took ~75 s. In the case of the PAN nanofiber mat with a thickness of $h = 0.25$ mm, in contrast to the previously discussed cases, it exhibited a relatively low spread-out diameter equal to ~7 times d_0 [Fig. 7(a)]. The time span of the maximum spreading configuration was ~70 s, which led to the longest measured entire evaporation time of 85 s.

The large differences in the maximum spreading diameter for the thin PAN + CB mat compared with the thinnest PAN mat can be explained by different properties of the two materials. By adding carbon black particles to the polymer solution, the roughness of individual nanofibers is increased (compare Figs. 1 and 2). The wettability properties are also affected by the carbon black particles.

The second parameter that was varied in these experiments was the initial foil temperature. Water penetration and spreading inside the mats occur for all nanofiber mats for initial foil temperatures up to 120 °C. As the initial foil temperature increased, the maximum spreading diameter as well as the evaporation time decreased, because the evaporation rate increased. The overall pattern of water spreading inside nanofiber mats was not affected by the initial foil temperature, as Figs. 8(a) and 8(b) show in comparison with Fig. 7(a).

For $h = 1.05$ mm at all initial temperatures, the drops spread very rapidly inside the mats and the dependence of the diameter of the cooled area on time had an almost parabolic shape over the entire process [Fig. 8(b)]. On the other hand, for a lower mat thickness of $h = 0.25$ mm, water spreads with a lower speed inside the mats and $d_{n,\max}$ is smaller for the investigated temperatures [Fig. 8(a)]. Moreover, not only were the curves $d_n(t)$ similar at increasing foil temperatures but also the wetted spot shapes were similar at the moment of the largest spread-out. Note the difference between the curves $d_n(t)$ for the two initial temperatures 60 and 80 °C in Fig. 8(a). At these temperatures the $d_n(t)$ curves are almost identical up to $t = 50$ s, whereas the evaporation time is significantly shorter for 80 °C. A reduction of the maximum diameter becomes visible only at

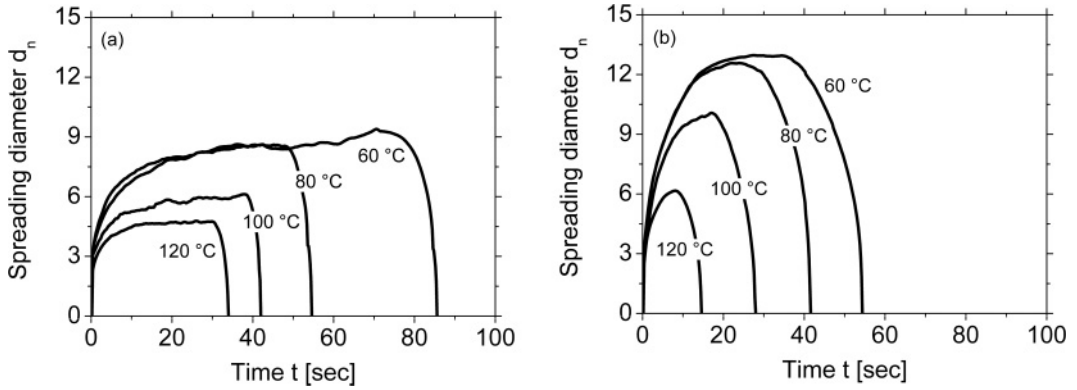

FIG. 8. Spreading diameter vs time for different initial foil temperatures. (a) PAN nanofiber mat with a thickness of $h = 0.25$ mm; (b) PAN with $h = 1.05$ mm.

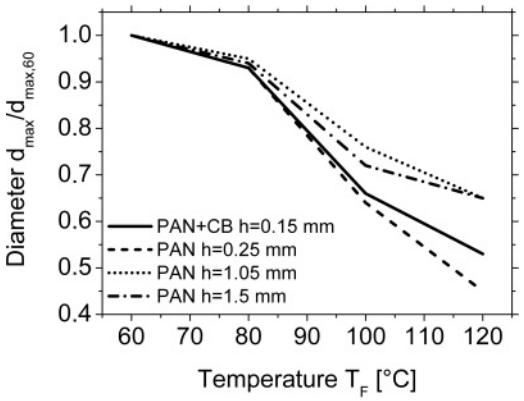

FIG. 9. Reduction of the relative maximum spreading diameter with increasing initial foil temperature.

~100 °C. This result can be explained by the intensification of the evaporation process at higher temperatures. This is further corroborated by Fig. 9, where d_{max} normalized by $d_{max,60}$ (at an initial temperature 60 °C), $d_{max}/d_{max,60}$, is plotted versus the initial foil temperature T_F.

The data that allow evaluation of the relation between the maximum spreading diameter, the mat thickness, and the corresponding evaporation time in the temperature range of 60–120 °C are shown in Fig. 10. It is seen that in the range of 60–100 °C there exists an optimal mat thickness of ~1 mm, which corresponds to the shortest evaporation time, hence the highest heat flux. Moreover, in the temperature range 60–120 °C there exists a mat thickness corresponding to a maximal value of d_{max}. It can be seen that, apart from the experiment performed at 120 °C, the evaporation time decreases with increasing maximum spreading diameter at a constant initial foil temperature. This can be explained by the increase of the liquid-gas interface area with an increase of the spreading diameter. The total evaporation rate increases and the evaporation time decreases with an increase of the liquid-gas interface area. The change of the trend for the initial foil temperature of 120 °C can be explained by the possible inception of boiling in the nanofiber mat. One conceivable reason for the nonmonotonic dependence of the maximum spreading diameter on the mat thickness can be the different impregnation behavior for thin and thick mats. In the case of thin mats the impregnation is mainly two-dimensional, because the thin mats are filled during drop impact through the entire depth. For mats thicker than $h = 1$ mm the impregnation process can be assumed to be three-dimensional, where wettability-driven filling in the third direction (in depth) occurs. With increasing mat thickness, the moisture flux in the depth direction increases and d_{max} decreases. The decrease of the maximum spreading diameter with decreasing mat thickness for the thin mats can be attributed to the wall effects.

The third parameter that was varied in the experiments was the impact height H and the corresponding drop impact velocity. It was observed that this parameter mainly influenced the drop spreading before the contact line had been pinned, rather than further mat imbibition. It is known that, in the case of drop impact onto a smooth dry substrate, increasing the impact velocity leads to the enlargement of the spreading diameter [14]. However, as seen in Fig. 11, the rate of water imbibition and evaporation inside nanofiber mats were almost unaffected by the impact velocity at different initial foil temperatures.

B. Cooling efficiency

Figures 12(a) and 12(b) show the foil temperatures at the impact axis for different nanofiber mats and the initial foil temperatures 60 and 100 °C. It can be seen that the foil temperature underneath the impact point drops almost instantaneously by ~25 °C for the initial foil temperature of 60 °C and by ~45 °C for 100 °C. After that, it stays almost constant during the whole evaporation process. It is emphasized that the minimum temperature at which the evaporation takes place is between 3 and 5 °C lower for all nanofiber mats than in the case of an uncoated steel foil. This is demonstrated in Fig. 13(a). Furthermore, the evaporation time is significantly shorter for all nanofiber mats than that for an uncoated steel foil, as is seen in Fig. 13(b). This diagram also elucidates the correlation between the maximum spreading diameter and the evaporation time. The samples in Fig. 13(b) are the same as in Fig. 7(a), from which the maximum diameters of the cooled area can be determined.

The evaporations times in the case of the PAN+CB mat with a thickness of $h = 0.15$ mm are the shortest ones for all temperatures, while at the same time this mat leads to the largest spreading diameters for all temperatures. The same observation is relevant for all the other mats, i.e., the larger

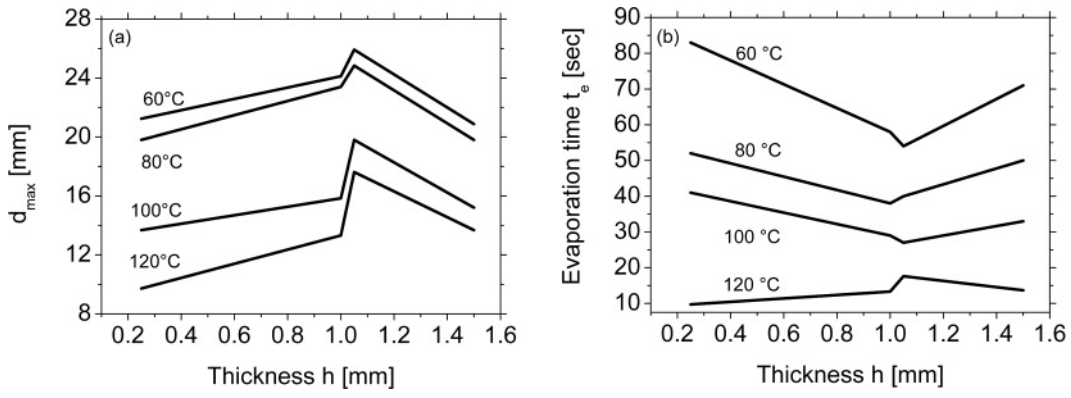

FIG. 10. (a) Maximum spreading diameter and (b) the corresponding evaporation time vs nanofiber mat thickness.

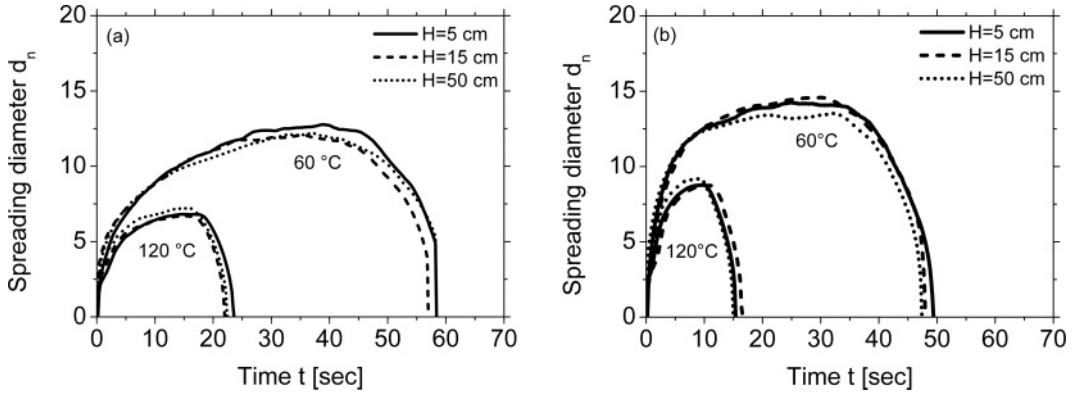

FIG. 11. Spreading diameter vs time for different impact heights. (a) PAN + CB nanofiber mat with thickness $h = 0.15$ mm; (b) PAN with $h = 1.00$ mm.

spreading diameters result in shorter evaporation times, as is also corroborated by Fig. 7(a).

At higher foil temperatures 220 and 260 °C, the temperature drop immediately underneath the impacting point can be as high as 140 and 180 °C, respectively.

IV. EVALUATION OF THE HEAT FLUX AND COMPARISON WITH THE EXPERIMENT

A. Water spreading and penetration into pores

The velocity of penetration of liquid into pores of nanofiber mats was studied first in Ref. [9] in the framework of the planar problem using the Cauchy formula from the complex analysis, which was reduced in that case to Poisson's integral formula for the upper half-plane. In the present section, a more realistic axisymmetric case of dynamic penetration of liquid is tackled. In our experiments drop diameters are typically of the order of $d_0 \approx 10^{-1}$ cm, whereas the pore sizes are of the order of 10^{-3} cm. Therefore, the drop impact onto a single pore can be imagined as an abrupt impact of a solid wall with a cylindrical orifice in the middle onto an upper half-space filled with water. A plane at $z = 0$ with the cylindrical orifice in the middle at $0 < r < a_0$ (where r and z are the radial and axial cylindrical coordinates centered at the orifice center and $a_0 = d_0/2$) imposes a pressure impulse on the liquid filling the upper half-plane $z > 0$. The pressure impulse $\Pi = \lim_{\substack{\tau\to 0\\ p\to\infty}} \int_0^\tau \Delta p\, dt$

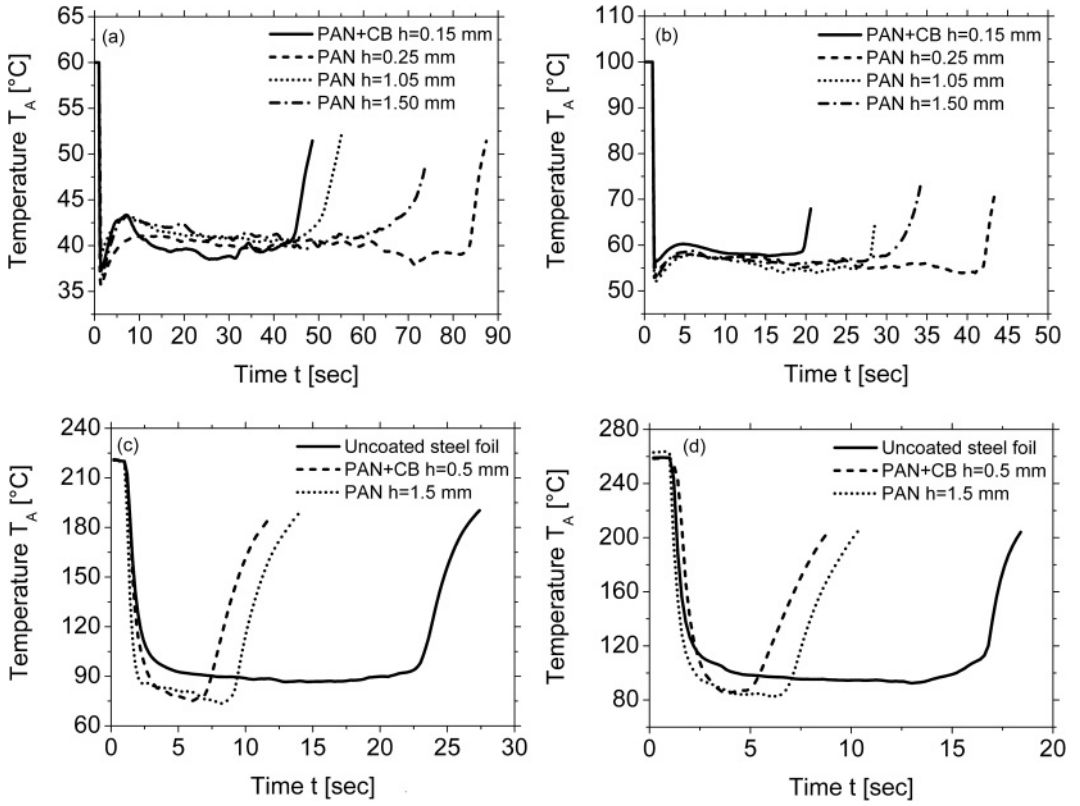

FIG. 12. Foil temperature under the drop impact point, T_A, for different nanofiber mats and different initial temperatures. (a) The initial foil temperature $T_{\text{foil,init}} = 60$ °C; (b) $T_{\text{foil,init}} = 100$ °C; (c) $T_{\text{foil,init}} = 220$ °C; (d) $T_{\text{foil,init}} = 260$ °C.

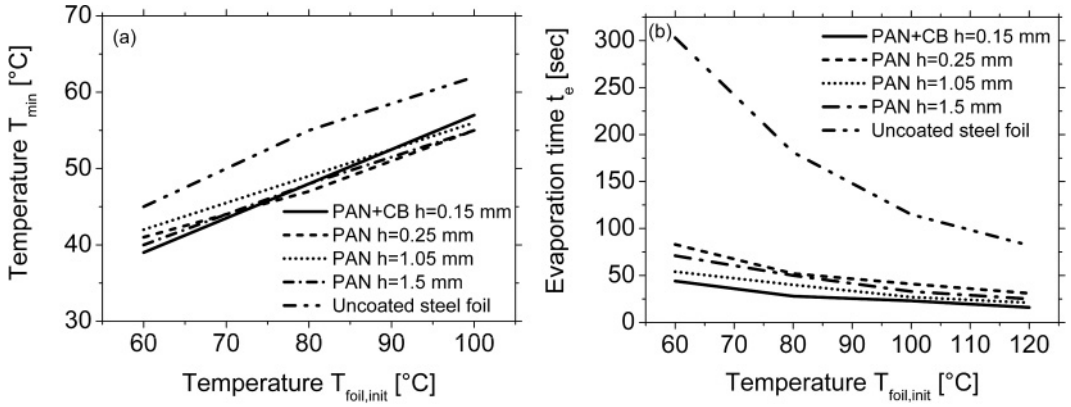

FIG. 13. Cooling efficiency of nanofiber mats as compared to the uncoated steel foil. (a) The minimum temperature and (b) the evaporation time vs the initial foil temperature.

(where pressure $\Delta p \to \infty$ and the impact duration $\tau \to 0$) is of the order of 1. The pressure impulse is applied at $r \geqslant a_p$, $z = 0$ to the liquid filling the upper half-plane, where a_p is the pore radius. Flows arising in response to the pressure impulse are known to be potential, with flow potential $\phi = -\Pi/\rho_w$ being a harmonic function [15] (ρ_w is liquid, water, density). Its value over the solid wall $r \geqslant a_p$, $z = 0$ at the moment of impact was evaluated in Ref. [9] as $\varphi = -V_0 d_0$, where V_0 is the drop impact velocity.

The axisymmetric Laplace equation for the potential reduces to

$$\frac{1}{r}\frac{\partial}{\partial r}\left(r\frac{\partial \varphi}{\partial r}\right) + \frac{\partial^2 \varphi}{\partial z^2} = 0. \tag{1}$$

The solution for liquid is searched for $0 \leqslant r \leqslant \infty$ and $z \geqslant 0$, and the potential distribution in the liquid in contact with the wall is posed in the form

$$\varphi|_{z=0} = f(r) = \begin{cases} 0, & 0 \leqslant r < a_p, \\ -V_0 d_0, & a_p < r < \infty \end{cases} \tag{2}$$

(see Fig. 14).

The additional boundary conditions required are the following:

$$\varphi|_{r=0} < \infty \quad \text{and} \quad \varphi < \infty \text{ over } r \to \infty \quad \text{and} \quad z \to \infty. \tag{3}$$

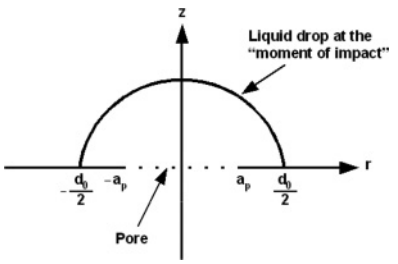

FIG. 14. Schematic of a liquid drop impact onto a single pore in the axisymmetric case.

To solve the problem (1)–(3) and find $\varphi(r,z)$, the method of separation of variables is applied. The solution of Eq. (1) satisfying the boundary conditions (3) has the following form:

$$\varphi = \int_0^\infty M_\nu e^{-\nu z} J_0(\nu r)\, d\nu, \tag{4}$$

where M_ν is an unknown function. This function can be determined from the boundary condition (2) using the following relation:

$$M_\nu = \nu \int_0^\infty f(\zeta)\zeta J_0(\nu\zeta)\, d\zeta = V_0 d_0 a_p J_1(\nu a_p), \tag{5}$$

where ζ is the dummy variable.

Then Eq. (4) yields

$$\varphi(r,z) = V_0 d_0 a_p \int_0^\infty J_0(\nu r) J_1(\nu a_p) e^{-\nu z} d\nu. \tag{6}$$

The velocity component $V_z = \partial\varphi/\partial z$, which yields at $z = 0$ using Eq. (6),

$$V_z|_{z=0} = -\frac{V_0 d_0}{a_p}\int_0^\infty \zeta J_1(\zeta) J_0(r\zeta/a_p)\, d\zeta. \tag{7}$$

At $z = 0$ and $r = 0$, correspondingly,

$$V_z\big|_{\substack{z=0\\r=0}} = -\frac{V_0 d_0}{a_p}\int_0^\infty \zeta J_1(\zeta)\, d\zeta. \tag{8}$$

However, according to Ref. [16],

$$\int_0^\infty \zeta J_1(\zeta)\, d\zeta = \int_0^\infty J_0(\zeta)\, d\zeta = 1. \tag{9}$$

Then Eqs. (8) and (9) yield

$$V_z\big|_{\substack{z=0\\r=0}} = \frac{-2V_0 d_0}{d_p}, \tag{10}$$

where the pore diameter $d_p = 2a_p$.

The velocity minimum is expected at the pore center, where $|(V_{z,\text{pore}})_{\min}| = U$,

$$U = \frac{2V_0 d_0}{d_p}. \tag{11}$$

As expected, in the axisymmetric case (11), the value of U is even higher than that for the planar case in Ref. [9], where it was $U = (4/\pi)(V_0 d_0)/d_p$.

According to the results obtained, the r component of the velocity vector over the opening vanishes, i.e., the flow through it right after drop impact will be strictly antiparallel to the z axis. The central part of the flow through the pore opening will not be affected by viscous forces when $\rho_w U^2 \gg \mu_w U/a_p$ (where ρ_w and μ_w are the liquid density and viscosity, respectively). That is equivalent to the condition where the Reynolds number $\mathrm{Re}_a = \rho_w U a_p/\mu_w \gg 1$. Taking for the estimate $d_0 \approx 10^{-2}$–10^{-1} cm, $d_p = 2a_p = 10^{-3}$ cm, and $V_0 = 1$ m/s, we find that $U = 10$–10^2 m/s $\gg V_0$ and for water $\mathrm{Re}_a = 10^2$–10^3. Therefore, in this case the high value of U will not be affected by viscosity even for such small pores, even though the flow close to the edges of the pore opening will be affected by viscosity. As mentioned in Ref. [9], drop penetration simultaneously in several pores will diminish the value of U. Still, a large disparity between d_0 and d_p will result in $U \gg V_0$.

The high values of the velocity U compared to the drop impact velocity V_0 stem from the accumulation of the kinetic energy of a large mass of liquid in flow through a narrow pore, and are reminiscent of the formation of shaped-charge (Munroe) jets [9].

The predicted values of the flow velocity through the pore $U \sim 10$–10^2 m/s are much higher than the speed of the wettability-driven impregnation of pores given by the Lucas-Washburn formula [17]. Accordingly, filling pores in the nanofiber mat of thickness $h \approx 10^{-1}$–1 mm after drop impact takes no more than $t_f \approx h/U \approx 10^{-4}$ s. On the other hand, complete drop spreading over the mat lasts for $\sim t_s \approx d_0/V_0 \approx 10^{-3}$ s [14,18], which means that filling pores is an almost instantaneous process on the background of drop spreading ($t_f \ll t_s$).

B. Heat transfer

The characteristic time of cooling of the metal foil directly under the drop (cooling stage 1) is of the order of $t_{\mathrm{foil,init}} = h_f^2/\alpha_{\mathrm{steel}}$, where $h_f = 50$ μm is the foil thickness and $\alpha_{\mathrm{steel}} = 4 \times 10^{-6}$ m^2/s is the thermal diffusivity of steel. This time $t_{\mathrm{foil,init}} = 6 \times 10^{-4}$ s, which is shorter than the time of spreading, and thus cannot be a limiting factor for the foil cooling.

The characteristic time of drop heating can be estimated as $t_{\mathrm{drop,init}} = h_{\mathrm{drop}}^2/\alpha_w$, where $\alpha_w = 1.4 \times 10^{-7}$ m^2/s is the thermal diffusivity of water. The thickness of the spreading drop initially varies in time as $h_{\mathrm{drop}} \sim t^{-2}$ [19,20] and then reaches the residual value $h_{\mathrm{drop,resid}} \approx d_0\,\mathrm{Re}^{-2/5}$ [21], where the Reynolds number $\mathrm{Re} = d_0 V_0/\nu_w$, where ν_w is the liquid kinematic viscosity. Because the Prandtl number of water is larger than unity, the thickness of the thermal boundary layer in the droplet is smaller than the thickness of the viscous one. Therefore, the residual drop thickness can be used safely for the estimation of the initial drop heating. The residual film thickness of the drop under our experimental conditions is $\sim$75 μm. Therefore, the drop heating time can be evaluated as $t_{\mathrm{drop,init}} \sim 10^{-2}$ s.

TABLE I. The initial heat flux q_{init} (kW/cm^2) for PAN + CB coated foils.

Initial foil temperature	60 °C	80 °C	100 °C
Cooling rate of the foil, $\lvert dT/dt\rvert$ (deg/s)	5770	7170	12800
Heat flux (kW/cm^2)	0.12	0.14	0.26

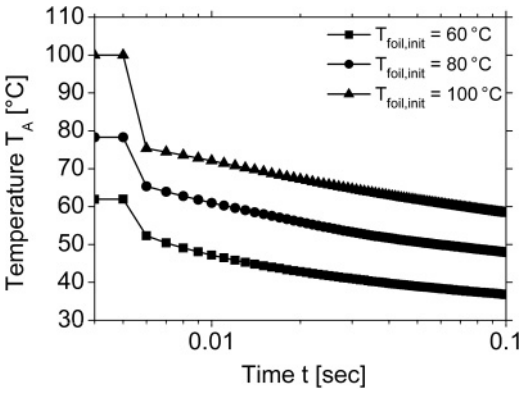

FIG. 15. Initial stage of cooling of a foil coated by the PAN + CB nanofiber mat.

The initial stage of foil cooling has been characterized by using time-resolved temperature measurements with a sampling rate of 1 kHz. The measurement results for PAN + CB nanofiber mats are shown in Fig. 15.

The average heat flux at the initial stage 1 can be estimated as $q_{\mathrm{init}} = \rho_{\mathrm{steel}} c_{\mathrm{steel}} h_{\mathrm{steel}} |dT_{\mathrm{steel}}/dt|$. Taking for the estimate $\rho_{\mathrm{steel}} = 8000$ kg/m^3, $c_{\mathrm{steel}} = 500$ J/(kg K), and $h_{\mathrm{steel}} = 50$ μm, we find the maximum measured values of q_{init} for PAN + carbon black coated foils in kW/cm^2 listed in Table I. It should be noted that the precision of the heat flux measurements at this stage is bounded by the sampling rate.

It is emphasized that the heat removed at stage 1 comprises only $\sim$0.1%–1% of heat, which will be removed after the whole drop evaporates. Indeed, $[\rho_{\mathrm{steel}} \pi a_{\mathrm{spot}}^2 h_{\mathrm{steel}} c_{\mathrm{steel}} (T_{\mathrm{foil},0} - T_{\mathrm{low,short}})]/[\rho_w (4/3)\pi a_0^3 L] = 10^{-3}$–$10^{-2}$, where a_0 is the initial drop radius, and L is latent heat of evaporation.

1. *Foil cooling at times t from the range $t_s < t < t_{\mathrm{drop,init}}$*

At times $t > t_s$ the temperature gradients in the foil under the spread-out drop can be neglected, and therefore the foil temperature can be estimated using the lumped capacity approximation. We assume that the main heat transfer mechanism is heat conduction between the cold water drop and the steel foil in the direction normal to the plane of the foil (the z direction). According to the estimates in Sec. IV A, we assume that for $t > t_s$ the nanofiber mats at the impact location are fully soaked with water. Because the volumetric fraction of the nanofibers is small, it can be assumed in our simplified analysis that the fully soaked nanofiber mats have the properties of water. The thermal conduction in the liquid is described using the transient one-dimensional thermal conduction equation

$$\frac{\partial T}{\partial t} = \alpha_w \frac{\partial^2 T}{\partial z^2}. \tag{12}$$

Equation (12) is solved subject to the following boundary condition at the foil:

$$\rho_{\mathrm{steel}} c_{\mathrm{steel}} h_{\mathrm{steel}} \frac{\partial T}{\partial t} = k_w \frac{\partial T}{\partial z} \quad \text{at} \quad z = 0, \tag{13}$$

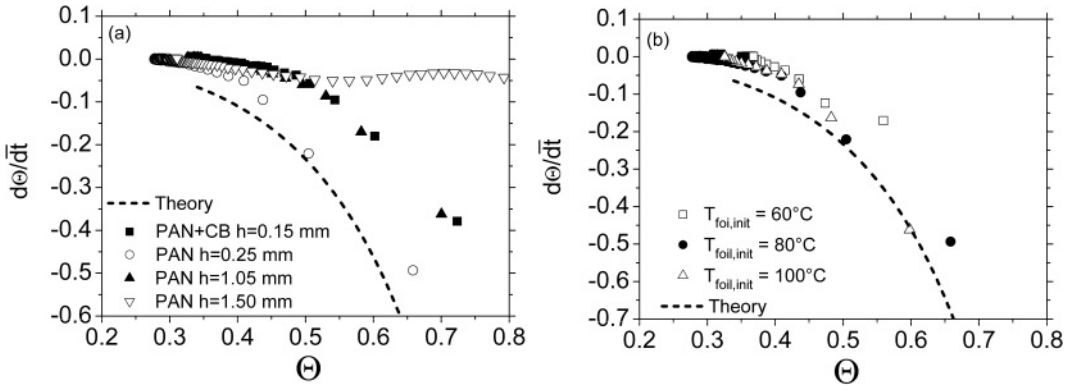

FIG. 16. Measured scaled rate of temperature evolution of the foil (the heat flux at the foil surface) in the range $t_s < t < t_{\mathrm{drop,init}}$ in comparison with the theoretical predictions (16). (a) Different nanofiber mats at the initial temperature 60 °C. (b) PAN nanofiber mat of $h = 0.25$ mm at different initial temperatures.

where k_w is the thermal conductivity of water, and ρ_{steel}, c_{steel}, and h_{steel} are the density, specific heat, and thickness of the steel foil, respectively.

Equations (12) and (13) can be written in the dimensionless form using the following dimensionless variables:

$$t = \bar{t}\frac{\alpha_w c_{\mathrm{steel}}^2 \rho_{\mathrm{steel}}^2 h_{\mathrm{steel}}^2}{k_w^2}, \quad z = \bar{z}\frac{\alpha_w c_{\mathrm{steel}} \rho_{\mathrm{steel}} h_{\mathrm{steel}}}{k_w}, \qquad \Theta(\bar{z},\bar{t}) = \frac{T - T_{\mathrm{drop},0}}{T_{\mathrm{foil},0} - T_{\mathrm{drop},0}}, \tag{14}$$

where subscript zero denotes the initial values.

The resulting dimensionless energy equation and boundary and initial conditions read

$$\frac{\partial\Theta}{\partial\bar{t}} = \frac{\partial^2\Theta}{\partial\bar{z}^2} \quad \text{for} \quad \bar{z} \geqslant 0, \quad \bar{t} \geqslant 0, \tag{15a}$$

$$\frac{\partial\Theta}{\partial\bar{t}} = \frac{\partial\Theta}{\partial\bar{z}} \quad \text{for} \quad \bar{z} = 0, \quad \bar{t} > 0, \tag{15b}$$

$$\lim_{\bar{z}\to\infty} \Theta = 0 \quad \text{for} \quad \bar{t} \geqslant 0, \tag{15c}$$

$$\Theta(\bar{z} = 0,\bar{t} = 0) = 1, \quad \Theta(\bar{z} > 0,\bar{t} = 0) = 1. \tag{15d}$$

The problem (15) is solved using the Laplace transform, which yields the following dimensionless dependence of $\Theta(\bar{z} = 0,\bar{t} > 0) = \Theta_{\mathrm{foil}}(\bar{t})$ on $\bar{t}$:

$$\Theta_{\mathrm{foil}} = 1 + \sum_{j=1}^{\infty} \frac{(-1)^j \bar{t}^{j/2}}{\Gamma(1 + j/2)}, \qquad \frac{d\Theta_{\mathrm{foil}}}{d\bar{t}} = \sum_{j=1}^{\infty} \frac{(-1)^j j\bar{t}^{j/2-1}}{2\Gamma(1 + j/2)}. \tag{16}$$

The theoretical prediction for the rate of Θ_{foil} variation (which is, in fact, the heat flux) is compared with the experimental data in Fig. 16 for different nanofiber mats and different initial temperatures of the foil. For the calculations the series (16) are truncated at the 51st term. The agreement of the theoretical results with the experimental data in Fig. 16 is reasonable. The closest agreement is observed for the PAN nanofiber mat of thickness $h = 0.25$ mm. Some deviation of the data from the theoretical predictions for other mats can be

TABLE II. Measured data for the wet spot radius a_{spot}, and wet spot temperatures $T_{\mathrm{low,short}}$ and $T_{\mathrm{low,plateau}}$.

	Initial temp. (°C)	a_{spot} (mm)	$T_{\mathrm{low,plateau}}$ (°C)	$T_{\mathrm{low,short}}$ (°C)	T_{low} (°C) Theory, Eq. (17)
PAN + CB	60	14.4	39	37	
$h = 0.15$ mm	80	13.5	48	45	
	100	9.5	58	56	
PAN	60	10.62	39	36	
$h = 0.25$ mm	80	9.9	47	44	
	100	6.84	56	53	
PAN	60	12.96	40	38	
$h = 1.05$ mm	80	12.42	45	43	
	100	9.9	56	53	
PAN	60	10.44	41	36	
$h = 1.5$ mm	80	9.9	49	44	
	100	7.6	57	53	
Bare steel foil	60	3	45	37	38
	80	3	56	47	46
	100	3	62	57	54

TABLE III. Measured and calculated evaporation time (s).

	60 °C Measured	60 °C Calculated	80 °C Measured	80 °C Calculated	100 °C Measured	100 °C Calculated
PAN + CB $h = 0.15$ mm	44	49	28	36	23	43
PAN $h = 0.25$ mm	83	77	52	53	41	55
PAN $h = 1.05$ mm	54	62	40	38	27	39
PAN $h = 1.5$ mm	71	86	50	56	33	52
Bare steel foil	303	266	181	166	115	105

explained by the influence of the mats on the effective thermal properties of the medium in contact with the steel foil.

2. *The lowest temperature of the foil at $t_s < t < t_{\mathrm{drop,init}}$*

The temperature of the foil T_{low} at times comparable with $t_{\mathrm{drop,init}}$ can be estimated from the energy balance, neglecting the heat losses to air and drop evaporation:

$$\rho_{\mathrm{steel}} c_{\mathrm{steel}} h_{\mathrm{steel}} (T_{\mathrm{foil},0} - T_{\mathrm{low}}) = \rho_w c_w h_{\mathrm{drop,resid}} (T_{\mathrm{low}} - T_{\mathrm{drop},0}), \tag{17}$$

where the initial drop temperature is $T_{\mathrm{drop},0} = 25\,^{\circ}\mathrm{C}$ and c_w is the specific heat of water. The estimated values of T_{low} for the case of drop impact onto a bare steel foil are shown in Table II in comparison with the measured data. The agreement of T_{low} with the measured value $T_{\mathrm{low,short}}$ ($T_{\mathrm{low,short}}$ is the lowest temperature direclty after drop impact; cf. Fig. 12) is very good. In addition, Table II also contains the measured values of the temperature $T_{\mathrm{low,plateau}}$ corresponding to the temperature plateau in Fig. 12.

At the second stage, steel under the spread-out drop has the low plateau temperature $T_{\mathrm{low,plateau}}$ (cf. Fig. 12), and the cooling process becomes different: Heat is transferred mainly by conduction along the foil horizontally to the cold spot of radius a_{spot} at the center. This heat transfer sustains evaporation of the main part of the drop on the cold spot, and this is a long limiting process. Indeed, the thermal balance for such a process relates the conductive heat transfer to the latent heat of evaporation:

$$k_{\mathrm{steel}} \frac{(T_\infty - T_{\mathrm{low,plateau}})}{a_{\mathrm{spot}} \ln(W/a_{\mathrm{spot}})} 2\pi a_{\mathrm{spot}} h_{\mathrm{steel}} \Delta t \approx \rho_w \frac{4}{3} \pi a_0^3 L, \tag{18}$$

where k_{steel} is the thermal conductivity of steel, W is of the order of the foil size, and Δt the duration of drop evaporation.

Equation (18) yields

$$\Delta t = \frac{2}{3} \frac{\rho_w a_0^3 L \ln(W/a_{\mathrm{spot}})}{k_{\mathrm{steel}} h_{\mathrm{steel}} (T_\infty - T_{\mathrm{low,plateau}})}. \tag{19}$$

Taking for the estimate $\rho_w = 1000\ \mathrm{kg/m^3}$, $k_{\mathrm{steel}} = 16\ \mathrm{W/(m\,K)}$, $L = 2260\ \mathrm{kJ/kg}$, and $W = 2.5$ cm as the foil width, one finds from Eq. (19) the values of drop evaporation time Δt listed in Table III in comparison with the experimental results.

Equation (19) incorporates the effect of nanofibers through the value of a_{spot}. Nanofiber mats increase a_{spot} and thus decrease Δt. The agreement of the measured and predicted values of Δt is fairly good.

V. CONCLUSION

Drop spreading after impact on a polymer nanofiber mat is almost instantaneously followed by water penetration into pores, after which heat is removed from the underlying hot stainless-steel foil, corresponding to the latent heat of water evaporation in direct contact with the foil. At the first stage of cooling, the heat flux is of the order of up to $0.3\ \mathrm{kW/cm^2}$, which is characteristic of spray cooling in general. At the second stage, heat is removed by conduction along the foil toward the cold central spot, which appeared at stage 1, and only then is used for water evaporation. The drop imbibition and evaporation introduce a limiting stage that prolongs the drop evaporation process to several tens of seconds and diminishes the overall heat flux. It is expected that the limiting stage can be significantly shortened with highly conductive metal nanofibers instead of the polymer ones used in the present work. The work on drop cooling through metal nanofibers is currently underway and will be reported separately [22].

ACKNOWLEDGMENTS

The authors would like to thank Matthias Winter (TTD) and Olympia Kyriopoulos (SLA) for their help in the design and construction of the experimental setup. Support of the Center of Smart Interfaces (Technische Universität Darmstadt) is greatly appreciated. Y.Z. and A.L.Y. are also grateful for the partial support of their work by the National Science Foundation through the Grant No. CBET-0966764 and NASA through the Grant No. NNX10AR99G. I.V.R. and C.T. acknowledge partial support by DFG in the framework of the Collaborative Research Center Transregio 75, subproject A4.

[1] L. P. Yarin, A. Mosyak, and G. Hetsroni, *Fluid Flow, Heat Transfer and Boiling in Microchannels* (Springer, Berlin, 2009).

[2] S. G. Kandlikar and A. V. Bapat, Heat Transfer Eng. **28**, 911 (2007).

[3] J. Kim, Int. J. Heat Fluid Flow **28**, 753 (2007).

[4] Z. B. Yan, K. C. Toh, F. Duan, T. N. Wong, K. F. Choo, P. K. Chan, and Y. S. Chua, Appl. Therm. Eng. **30**, 1225 (2010).
[5] M. Visaria and I. Mudawar, IEEE Trans. Compon. Packag. Technol. **32**, 784 (2009).
[6] R. M. Manglik and M. A. Jog, J. Heat Transf. **131**, 121001 (2009).
[7] M. R. O. Panao and A. L. N. Moreira, Int. J. Therm. Sci. **48**, 1853 (2009).
[8] R. Srikar, T. Gambaryan-Roisman, C. Steffes, P. Stephan, C. Tropea, and A. L. Yarin, Int. J. Heat Mass Transf. **52**, 5814 (2009).
[9] A. N. Lembach, H. B. Tan, I. V. Roisman, T. Gambaryan-Roisman, Y. Zhang, C. Tropea, and A. L. Yarin, Langmuir **26**, 9516 (2010).
[10] D. H. Reneker, A. L. Yarin, E. Zussman, and H. Xu, Adv. Appl. Mech. **41**, 43 (2007).
[11] D. H. Reneker and A. L. Yarin, Polymer **49**, 2387 (2008).
[12] M. K. Tiwari, A. L. Yarin, and C. M. Megaridis, J. Appl. Phys. **103**, 044305 (2008).
[13] D. H. Reneker, A. L. Yarin, H. Fong, and S. Koombhongse, J. Appl. Phys. **87**, 4531 (2000).
[14] A. L. Yarin, Annu. Rev. Fluid Mech. **38**, 159 (2006).
[15] G. K. Batchelor, *Introduction to Fluid Dynamics* (Cambridge University Press, Cambridge, UK, 1967).
[16] I. S. Gradshteyn and I. M. Ryzhik, *Table of Integrals, Series and Products*, 7th ed. (Elsevier, Amsterdam, 2007).
[17] E. W. Washburn, Proc. Natl. Acad. Sci. **7**, 115 (1921).
[18] R. Rioboo, M. Marengo, and C. Tropea, Exp. Fluids **33**, 112 (2002).
[19] A. L. Yarin and D. A. Weiss, J. Fluid Mech. **283**, 141 (1995).
[20] I. V. Roisman, E. Berberović, and C. Tropea, Phys. Fluids **21**, 052103 (2009).
[21] I. V. Roisman, Phys. Fluids **21**, 052104 (2009).
[22] S. Sinha-Ray, Y. Zhang, and A. L. Yarin, Langmuir **27**(1), 215 (2011).